

Two-photon-induced photoluminescence imaging of tumors using near-infrared excited gold nanoshells

Jaesook Park¹, Arnold Estrada¹, Kelly Sharp², Krystina Sang², Jon A. Schwartz²,
Danielle K. Smith³, Chris Coleman², J. Donald Payne²,
Brian A. Korgel³, Andrew K. Dunn¹, James W. Tunnell^{1*}

¹ Department of Biomedical Engineering, The University of Texas at Austin, Texas 78712

² Nanospectra Biosciences Inc., Houston, Texas, 77054

³ Department of Chemical Engineering, The University of Texas at Austin, 78712

*Corresponding author: jtunnell@mail.utexas.edu

Abstract: Gold nanoshells (dielectric silica core/gold shell) are a novel class of hybrid metal nanoparticles whose unique optical properties have spawned new applications including more sensitive molecular assays and cancer therapy. We report a new photo-physical property of nanoshells (NS) whereby these particles glow brightly when excited by near-infrared light. We characterized the luminescence brightness of NS, comparing to that of gold nanorods (NR) and fluorescent beads (FB). We find that NS are as bright as NR and 140 times brighter than FB. To demonstrate the potential application of this bright two-photon-induced photoluminescence (TPIP) signal for biological imaging, we imaged the 3D distribution of gold nanoshells targeted to murine tumors.

©2008 Optical Society of America

OCIS codes: (190.4180) Multiphoton processes; (250.5230) Photoluminescence

References and links

1. C. Loo, A. Lowery, N. Halas, J. West, and R. Drezek, "Immunotargeted nanoshells for integrated cancer imaging and therapy," *Nano Lett.* **5**, 709–711 (2005).
2. R. D. Averitt, D. Sarkar, and N. J. Halas, "Plasmon resonance shifts of Au-coated Au₂S nanoshells: insight into multicomponent nanoparticle growth," *Phys. Rev. Lett.* **78**, 4217–4220 (1997).
3. S. J. Oldenburg, R. D. Averitt, S. L. Westcott, and N. J. Halas, "Nanoengineering of optical resonances," *Chem. Phys. Lett.* **288**, 243–247 (1998).
4. S. J. Oldenburg, J. B. Jackson, S. L. Westcott, and N. J. Halas, "Light scattering from dipole and quadrupole nanoshell antennas," *Appl. Phys. Lett.* **75**, 2897–2899 (1999).
5. E. Prodan, and P. Nordlander, "Structural tunability of the plasmon resonances in metallic nanoshells," *Nano Lett.* **3**, 543–547 (2003).
6. L. R. Hirsch, R. J. Stafford, J. A. Bankson, S. R. Sershen, B. Rivera, R. E. Price, J. D. Hazle, N. J. Halas, and J. L. West, "Nanoscale imaging of chemical interactions: fluorine on graphite," *Proc. Natl. Acad. Sci. U.S.A.* **100**, 13549–13554 (2003).
7. H. Maeda, J. Fang, T. Inutsuka, and Y. Kitamoto, "Vascular permeability enhancement in solid tumor: various factors, mechanisms involved and its implications," *Int. Immunopharmacol.* **3**, 319–328 (2003).
8. D. P. O'Neal, L. R. Hirsch, N. J. Halas, J. D. Payne, and J. L. West, "Photo-thermal tumor ablation in mice using near infrared-absorbing nanoparticles," *Cancer Lett.* **209**, 171–176 (2004).
9. A. M. Gobin, M. H. Lee, N. J. Halas, W. D. James, R. A. Drezek, and J. L. West, "Near-Infrared Resonant Nanoshells for Combined Optical Imaging and Photothermal Cancer Therapy," *Nano Lett.* **7**, 1929–1934 (2007).
10. M. Ferrari, "Cancer nanotechnology: opportunities and challenges," *Nat. Rev. Cancer* **5**, 161–171 (2005).
11. C. Loo, A. Lin, L. Hirsch, M. H. Lee, J. Barton, N. Halas, J. West, and R. Drezek, "Nanoshell-enabled photonics-based imaging and therapy of cancer," *Technol. Cancer Res. Treat.* **3**, 33–40 (2004).
12. C. Loo, L. Hirsch, M. H. Lee, E. Chang, J. West, N. Halas and R. Drezek, "Gold nanoshell bioconjugates for molecular imaging in living cells," *Opt. Lett.* **30**, 1012–1014 (2005).
13. C. Wu, X. Liang, and H. Jiang, "Metal nanoshells as a contrast agent in near-infrared diffuse optical tomography," *Opt. Commun.* **253**, 214–221 (2005).

14. A. Mooradian, "Photoluminescence of metals," *Phys. Rev. Lett.* **22**, 185–187 (1969).
15. K. Imura, T. Nagahara, and H. Okamoto, "Near-field two-photon-induced photoluminescence from single gold nanorods and imaging of plasmon modes," *J. Phys. Chem. B* **109**, 13214–13220 (2005).
16. G. T. Boyd, Z. H. Yu, and Y. R. Shen, "Photoinduced luminescence from the noble metal and its enhancement on roughened surfaces," *Phys. Rev. B* **33**, 7923–7936 (1986).
17. H. Wang, T. B. Huff, D. A. Zweifel, W. He, P. S. Low, A. Wei, and J. Cheng, "In vitro and in vivo two-photon luminescence imaging of single gold nanorods," *Proc. Natl. Acad. Sci. U.S.A.* **102**, 15752–15756 (2005).
18. N. J. Durr, T. Larson, D. K. Smith, B. A. Korgel, K. Sokolov, and A. Ben-Yakar, "Two-photon luminescence imaging of cancer cells using molecularly targeted gold nanorods," *Nano Lett.* **7**, 941–945 (2007).
19. W. R. Zipfel, R. M. Williams, and W. W. Webb, "Nonlinear magic: Multiphoton microscopy in the biosciences," *Nat. Biotechnol.* **21**, 1369–1377 (2003).
20. D. G. Duff, A. Baiker, and P. P. Edwards, "A new hydrosol of gold clusters. 1. formation and particle size. Variation," *Langmuir* **9**, 2301–2309 (1993).
21. X. H. Huang, I. H. El-Sayed, W. Qian, and M. A. El-Sayed, "Cancer cell imaging and photothermal therapy in the near-infrared region by using gold nanorods," *J. Am. Chem. Soc.* **128**, 2115–2120 (2006).
22. M. R. Beversluis, A. Bouhelier, and L. Novotny, "Continuum generation from single gold nanostructures through near-field mediated intraband transitions," *Phys. Rev. B* **68**, 115433-1-115433-10 (2003).
23. N. Nishimura, C. B. Schaffer, B. Friedman, P. S. Tsai, P. D. Lyden, and D. Kleinfeld, "Targeted insult to subsurface cortical blood vessels using ultrashort laser pulses: three models of stroke," *Nat. Methods* **3**, 99–108 (2006).

1. Introduction

Gold nanoshells (NS) have gained interest as a novel platform for integrated cancer imaging and therapy due to their highly desirable spectral and molecular properties [1]. NS consist of a dielectric silica core covered with a gold shell, whereby the core/shell ratio can tune the surface plasmon resonance (SPR) to the near-infrared (NIR) where light penetration in tissue is optimal [2–5]. Given their gold surface, NS are molecularly stable, provide surface chemistries suitable for bioconjugation of cancer targeting biomarkers and efficiently convert light to heat for photothermal therapy.

Applications of NS have recently been demonstrated for *in vivo* targeting and photothermal therapy of murine tumors. Hirsch *et al.* [6] demonstrated NS targeting of tumor tissue via the enhanced permeability and retention (EPR) effect [7], a common drug delivery mechanism used for macromolecules. NS in solution delivered intravenously will preferentially accumulate at the tumor site by extravasating through leaky neo-vasculature. Subsequent NIR irradiation of the tumor site leads to photothermal ablation and eventual tumor clearance. Several studies have demonstrated the efficiency of this treatment in murine survival studies [8, 9].

Much of the promise in this and related nanotechnologies rely not only on their therapeutic effect but also their diagnostic potential [10]. To be effective diagnostic tools, we require effective techniques to detect and image these particles in tissue at both the macroscopic and the microscopic scale. Ferrari *et al.* describes these combined technologies as "nanovectors" that incorporate mechanisms for targeting, imaging, and therapy into a single agent. While many current platforms combine multiple technologies to achieve this, direct imaging of the therapeutic agent would surpass the need for adding additional components to these nanovectors.

Previous efforts for direct imaging NS have focused on scattering and absorption based contrast. Loo *et al.* demonstrated *in vitro* dark field microscopy of molecularly targeted NS attached to HER2-positive SKBR3 breast cancer cells as an application of scattering based contrast agent [11, 12]. Gobin *et al.* showed the use of NS as contrast agents for optical coherence tomography and quantified increased scattering intensity from NS-injected tumor [9]. Wu *et al.* demonstrated a NS based absorption agent for NIR diffuse optical tomography, and their tissue phantom results showed that NS are a much more efficient absorption contrast agent than indocyanine green molecules [13]. While these imaging techniques show great

promise, direct luminescence based imaging of metal nanoparticles may provide increased background rejection and signal-to-noise ratios enabling imaging deep within bulk tissue.

Historically, direct luminescence measurements from metals have been difficult to measure given their small quantum yields. Single-photon induced photoluminescence (SPIP) from gold and copper was first reported by Mooradian in 1969 [14]. This researcher described the photoluminescence process as the radiative recombination of excited electrons in the sp-band and holes in the d-band [15]. Subsequently, Boyd *et al.* [16] investigated SPIP and two-photon-induced photoluminescence (TPIP) from smooth and roughened metal surfaces. They report significant enhancement of TPIP intensity ($\sim 10^6$) from the roughened surfaces of copper and gold and attribute this enhancement to coupling of the localized surface plasmon resonances. With recent advancements in the fabrication of nanoparticles with strong SPR in the NIR, SPR enhancement of luminescence of nanoparticles has recently been extended for biological imaging. Wang *et al.* demonstrated strong NIR excited TPIP from a single gold nanorod (NR) that was 58 times brighter than a single rhodamine 6G molecule [17]. These strong TPIP signals have been used to image molecularly targeted NR for cancer cells *in vitro* [18] and to image NR flowing in a mouse ear blood vessel *in vivo* [17].

In this study, we report strong NIR excited TPIP from silica/gold NS. We compare the luminescence brightness from NS to that of NR and fluorescent beads (FB). We find that the brightness of NS and NR are approximately equal while FB require 12 times higher power than NS to emit the same fluorescence intensity. This strong TPIP signal enables use of NS as biological imaging agents. We demonstrate this luminescence for imaging the 3D distribution of NS in tumors using a NIR laser scanning multi-photon microscope.

2. Materials and methods

2.1 Custom-built multi-photon microscope

Measurements of TPIP from NS were performed using the custom built NIR laser scanning multi-photon microscope illustrated in Fig. 1. A femtosecond Ti:Sapphire laser (Mira 900, Coherent Inc.) was used as the TPIP excitation source, and the power was modulated using an acousto-optic modulator (23080-1, NEOS Technologies). Because the distance from the laser to the objective was large (~ 8 m), beam conditioning optics were used to reduce beam size of the diverging beam. A pick-off mirror (reflectance 1 %) sampled the beam prior to the scanning optics, and the beam power was monitored using a photodiode calibrated for monitoring the power delivered to the objective's back aperture. The focal volume of the objective lens (40x, 0.75NA, water emersion, Zeiss) was scanned along the sample in the x-y plane using a pair of galvanometric scanning mirrors (6215HB, Cambridge Technology Inc.). The objective lens used for this study produced a focal spot with a beam waist of $0.46 \mu\text{m}$ and a focal volume of 0.55 fl [19]. We measured the beam pulse width as approximately 300 fs at the pick-off mirror.

TPIP from the NS was collected using an epicollection geometry and reflected by a dichroic beam splitter (FF735-Di01, Semrock) toward the photomultiplier tube (PMT) (H7422P-50, Hamamatsu). A lens was then placed after the dichroic to increase collection efficiency. Additionally, a short-pass, laser blocking emission filter (FF01-750/SP-25, Semrock Inc.) was used to pass the luminescence while blocking excitation scatter from reaching the PMT. For the purpose of these measurements, we used three band-pass filters with center wavelength of 510, 610 and 700 nm (for fluorescein, NS and NR, respectively) (Chroma Technology).

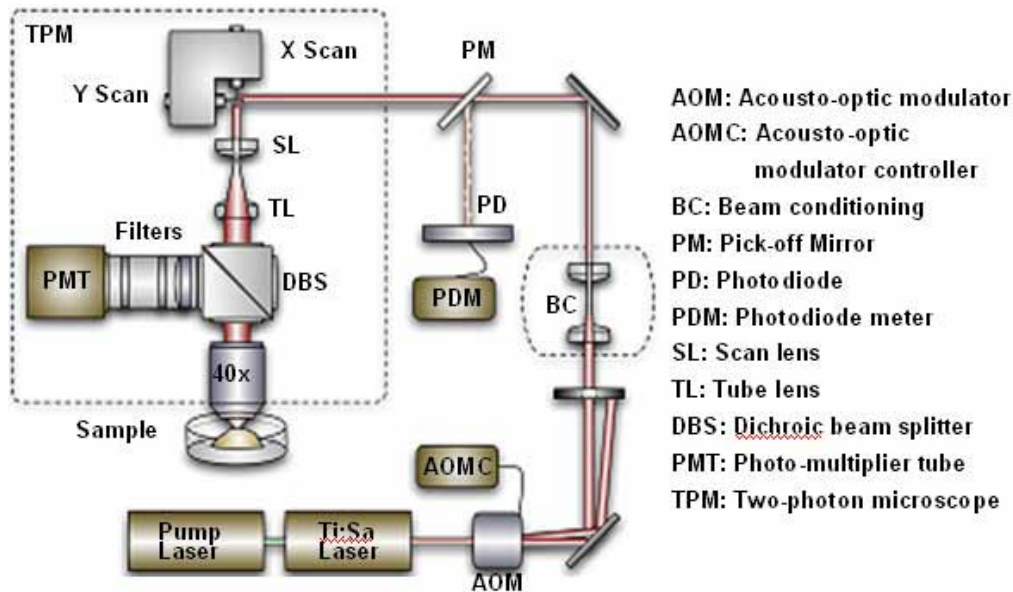


Fig. 1. Schematic of the custom built NIR laser scanning multi-photon microscope.

2.2 Synthesis of gold nanoshells and nanorods

NS were synthesized using the seed-mediated method. The core of the particle (120 nm diameter) was made of colloidal silica. Nanoscale gold colloid (1-3 nm) was grown using the method of Duff *et al.* [20] This colloid was aged for 2 weeks at 4 °C; then, aminated silica particles were added to the gold colloid suspension. Gold colloid adsorbed to the amine groups on the silica surface, resulting in a silica particle covered with gold colloid as nucleating sites. Gold-silica NS were then grown by reacting hydrogen tetrachloroaurate (III) hydrate with the silica-colloid particles in the presence of formaldehyde. This process reduced additional gold onto the adsorbed colloid, which act as nucleation sites, causing the surface colloid to grow and coalesce with neighboring colloid, forming a complete metal shell. NS formation and dispersion in solution were assessed using a UV-Vis spectrophotometer. NS for this study were designed to have 120 nm core diameters and a 15 nm thick shell resulting in an absorption peak between 780 and 800 nm. For *in vivo* use, a layer of 5,000 MW polyethyleneglycol was added to the exterior shell through a thiol bond, and the particles were suspended in an iso-osmotic solution of 10 % trehalose. To prevent changes in osmotic pressure in the bloodstream, 0.9 % saline is commonly used; however, NS tend to aggregate in the presence of salt. Therefore, isotonic sugar solution, trehalose, was used in this study. A transmission electron microscopy (TEM) image of synthesized NS and its extinction spectra are shown in Fig. 2(a) and (b).

NR were synthesized in a two-step procedure adapted from the work of Huang *et al* [21]. Small (~ 1.5 nm) gold seeds were prepared, and these seeds were injected into a growth solution containing silver and gold ions, ascorbic acid, and two surfactants, BDAC (benzyltrimethylammonium chloride) and CTAB (cetyltrimethylammonium bromide). Seeds were nucleated by reducing the gold in an aqueous solution of hydrogen tetrachloroaurate (III) hydrate (0.01 M, 250 μ l) and hexadecyltrimethylammonium bromide (0.1 M, 9.75 ml) with cold sodium borohydride (0.01 M, 600 μ l). The growth solution was prepared by mixing aqueous solutions of BDAC (0.15 M, 5 ml), CTAB (0.2 M, 5 ml), silver nitrate (0.004 M, 250

μl), hydrogen tetrachloroaurate (III) hydrate (0.01 M, 500 μl), and ascorbic acid (0.0788 M, 70 μl). To initiate the growth of NR, 8 μl of seed solution was added to the growth solution and then, NR were purified by two-cycle centrifugation and redispersion in ultra-pure water. The NR were isolated in the precipitate, and excess CTAB was removed in the supernatant. A TEM image of the NR and the extinction spectra with a second plasmon peak at 813 nm are shown in Fig. 2(c) and (d), respectively.

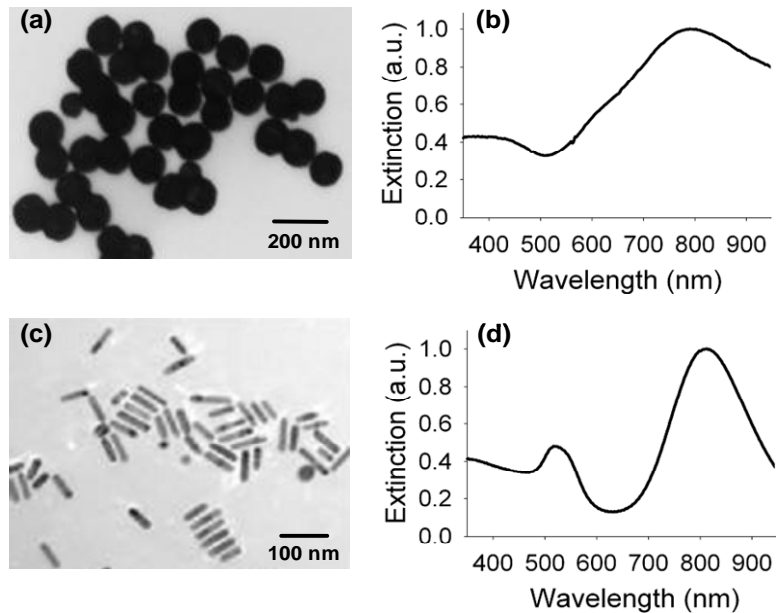


Fig. 2. Photo-physical properties of the gold nanoshells and nanorods used for this study. (a) TEM image of synthesized gold nanoshells. (b) Extinction spectra of gold nanoshells. (c) TEM image of nanorods. (d) Extinction spectra of gold nanorods. (Scale bar: 200 nm (a) and 100 nm (c))

3. Results

3.1 Quadratic dependence of luminescence on incident laser power and luminescence emission spectrum

NS TPIP was confirmed by measuring the quadratic dependence of TPIP emission intensity on the excitation power. NS suspended in trehalose solution ($2.85 \times 10^8 \text{ NS}/\mu\text{l}$) were mixed with 2 % (wt/wt) gelatin (G9382, Sigma) solution ($1.14 \times 10^6 \text{ NS}/\mu\text{l}$) and placed onto a glass slide. Luminescence intensities from NS solution were obtained using the custom built multi-photon microscope described in section 2.2. Incident laser power was monitored using a photodiode and calibrated to determine the power (130 μW to 470 μW) delivered to the sample. Luminescence intensities were measured by the PMT. Figure 3(a) illustrates the quadratic dependence of TPIP intensity on the input power with an average slope value of 2.00, confirming the two-photon luminescence process. This slope varied from 1.96 to 2.05 for the three replicate of this experiment. Figure 3(b) shows the TPIP emission spectrum with a peak emission at 610 nm, which was detected by an optical fiber coupled to a spectrometer (USB4000, Ocean Optics). The general shape of this emission spectrum is similar to that reported from NR [18] and roughened gold surfaces [22]; however, the location of the peak

varies between the different samples. This likely occurs from variations in the location of the plasmon resonances for the different structures.

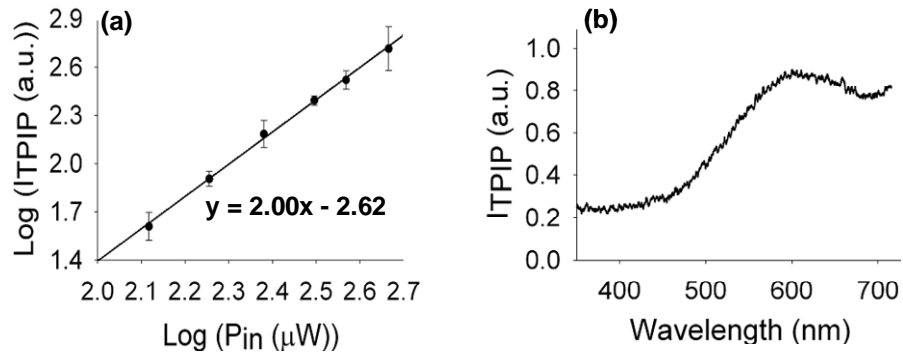


Fig. 3. Nonlinear property of two-photon-induced photoluminescence and emission spectrum. (a) Quadratic dependence of luminescence intensity on the excitation power at 780 nm. Error bars represent standard deviation ($n=3$). (b) Luminescence emission spectrum of gold nanoshells in solution.

3.2 Brightness characterization

To quantify the luminescence brightness from NS, we compared NS TPIP to that of NR and FB. We used the same NR described above. For FB, we used 100 nm diameter polystyrene beads covered with fluorescein molecules (F8803, Invitrogen). FB have been widely used as fluorescent probes in multi-photon microscopy due to their brightness. A single FB particle used in this study is equivalent to 7.4×10^3 fluorescein molecules. The solutions of FB (3.60×10^5 FB/ml), NR (1.35×10^6 NR/ml) and NS (1.14×10^6 NS/ml) were mixed with gelatin (2 % wt/wt) and dispersed on to glass slides. Then, fluorescence and luminescence intensities from FB, NR and NS were obtained by imaging the individual particles. NR and NS measurements were performed under the same condition with incident power of 457 μ W and excitation at 780 nm. Measured average intensities of NS ($n=39$) and NR ($n=34$) were 0.500 ± 0.053 V and 0.575 ± 0.079 V, respectively. In this way, we found that the brightness ratio of NS to NR is 1 to 1.15, indicating the brightness of NS's are on the same order of magnitude as that of NR's. As NR two-photon action cross sections (2,320 GM; 1 GM (Göppert-Mayer unit) = 10^{-50} (cm⁴·s)/photon) have been deemed as comparable to that of quantum dots (2,000-47,000 GM) [17], this indicates NS exhibit bright luminescence signals with potential for biological imaging applications.

We found the relative brightness of the FB to be much less than that of the NS. Therefore, for the studies comparing the brightness of NS to FB, we varied laser incident power. We determined that FB ($n=12$, average intensity of 0.175 ± 0.028 V) required an incident power of 3.16 mW to achieve the same output intensity for NS ($n=39$, average intensity of 0.175 ± 0.018 V) excited with 270 μ W. Intensity values of NS luminescence at 270 μ W were calculated by the quadratic relationship between incident power and emission intensity, which is illustrated in Fig. 3(a). Thus, FB required approximately 12 times more incident power to achieve the same brightness in the image, and these measurements indicate that NS produce 140 times brighter signal than FB with the same incident power. These results suggest that the strong TPIP of NS can be used as effective multi-photon contrast agents for biological imaging.

3.3 Damage threshold of gold nanoshells

As it is possible to damage NS at high incident powers, we determined the damage threshold to confirm that signals from luminescence measurements did not result from damaging, burning and melting NS. We applied incident laser powers of 1.5 and 4.5 mW to NS samples and obtained TEM images to verify their conformation. Figure 4 shows various TEM images of NS for the two incident laser powers. NS were heavily deformed for 4.5 mW irradiation (Fig. 4(a)-(d)), while 1.5 mW laser power did not lead to morphological changes (Fig. 4(e)). With an energy dispersive spectrometer (INCA EDS, Oxford Instruments), NS damage was analyzed by measuring the chemical elements in nanoshell solution. No silica peaks were found in the case of 1.5 mW irradiation, meaning gold shells were not melted and peeled off from the silica core. Figure 4(a)-(d) show various conformations of melted gold shells and silica cores due to the high incident power and (e) illustrates intact NS, suggesting incident powers under 1.5 mW are below the NS damage threshold. The laser power (130 μ W to 830 μ W) used for measuring luminescence intensities and the emission spectrum in this study was well below 1.5 mW.

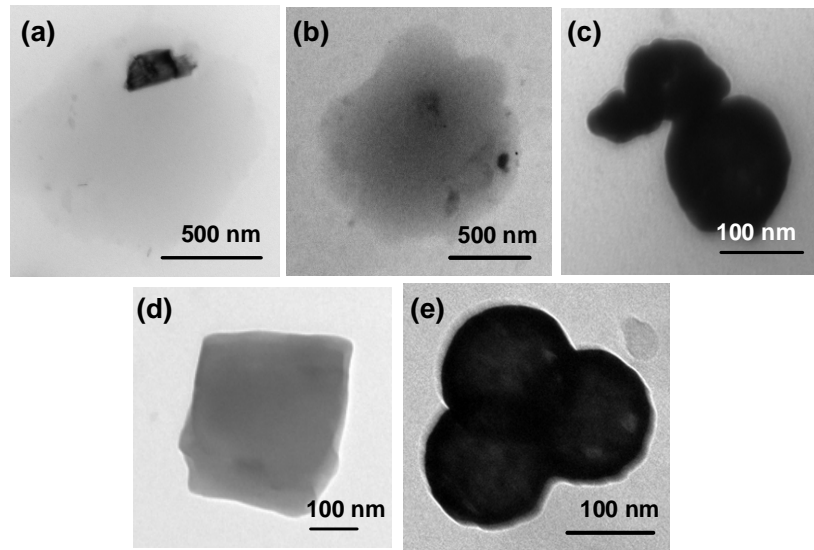


Fig. 4. TEM images of nanoshells irradiated with 4.5 mW and 1.5 mW incident laser powers. (a)-(d) Melted gold shells and silica cores after 4.5 mW irradiation. (e) Intact nanoshells after 1.5 mW irradiation. (Scale bar: 500 nm (a, b) and 100 nm (c-e))

3.4 Luminescence imaging

To demonstrate the potential of NS for multi-photon microscopy in bulk tissue, we imaged NS targeting of subcutaneous murine tumors. We used a subcutaneous xenograft tumor model in Balb/c mice inoculated with the CT26.WT cell line (ATCC #CRL-2638, mouse colon). Three groups of mice were selected for imaging when the tumors reached 5 mm diameter. Group 1 (n=3) received 4.5 μ l/g of NS solution standardized to an optical density of 100 at 800 nm (2.66×10^8 NS/ μ l) injected intravenously via the tail vein. Group 2 (n=3) served as the control and received a 4.5 μ l/g saline injection. Group 3 (n=2) received the NS solution (4.5 μ l/g) and a fluorescein-conjugated dextran (FD2000S, Sigma) solution (0.16 ml of a 2.5 % (wt/vol) solution) for visualization of blood vessels [23]. After 24 h following NS

injection and immediately after fluorescein injection, a skin flap with the tumor was excised from the mice to expose the subcutaneous side of the tumor. Then, TPIP images of the tumors were obtained using the multi-photon microscope. Luminescence from NS was visible in all mice of Group 1 and 3. In Fig. 5(a) and (c) show white light images of tumor samples, while Fig. 5(b) and (d) present TPIP images from the tumors. Whereas Fig. 5(d), the saline-injected animal, does not yield a TPIP signal, (b) shows strong TPIP signals from the tumor site, which verifies that luminescence-based imaging can be used to investigate accumulated NS at the tumor.

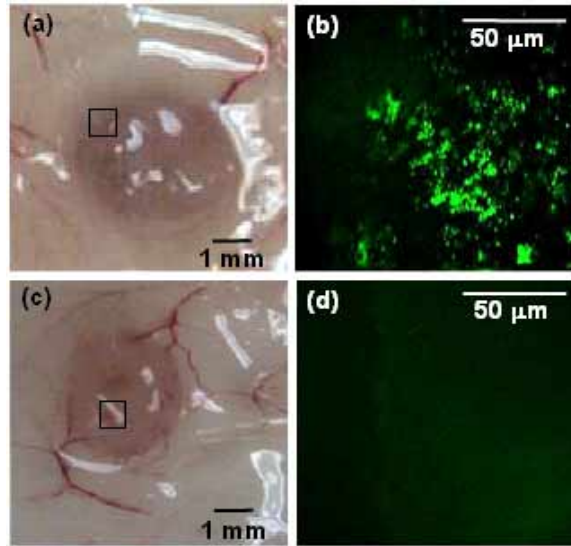


Fig. 5. Standard white light images and two-photon induced photoluminescence (TPIP) images from subcutaneous tumors. (a), (c) White light images of tumor with and without nanoshells. (b), (d) TPIP images from tumors with and without nanoshells. (Scale bar: 1 mm (a, c) and 50 μm (b, d))

As clinical applications of NS for cancer imaging and therapy have gained interest, efforts for understanding the kinetics of NS delivery and targeting of tumors has become more important. Therefore, we also examined the feasibility of using TPIP for imaging the distribution of NS in tumors. Figure 6(a) shows a 3D luminescence image of NS in the tumor of the first group of mice. 3D volume visualization of the cross-sectional luminescence images with 2 μm interval spacing was carried out using 3D data visualization software (Amira 4.1.2, Mercury Computer Systems). Figure 6(b) and (c) present the x-y (*en-face*) image stacked along z direction and x-z (cross-sectional) image stacked along y direction, respectively. The field of view was 124 μm x 124 μm and the imaging depth was 150 μm . These images demonstrate the ability of TPIP imaging of NS up to a depth of 130 μm in bulk tumor. In addition, these images illustrate the heterogeneous nature of NS distribution within a tumor site.

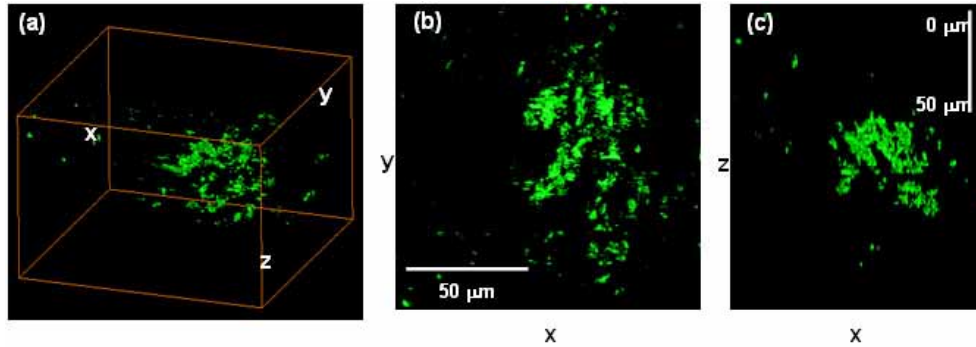


Fig. 6. Two-photon induced photoluminescence (TPIP) images of distribution of gold nanoshells in tumor. (a) (1.85 MB) A movie file of 3D luminescence images from nanoshell-injected tumor. (b) x-y (*en-face*) plane images of TPIP with field of view of $124\ \mu\text{m} \times 124\ \mu\text{m}$. (c) x-z (cross-sectional) plane images of TPIP in tumor from surface ($0\ \mu\text{m}$) down to $150\ \mu\text{m}$ deep. (Scale bar: $50\ \mu\text{m}$ (b, c))

For better understanding tumor-NS targeting, we imaged the blood vessels and NS simultaneously using fluorescein-conjugated dextran to label tumor vasculature. Using appropriate band-pass filters ($510\ \text{nm}$ for fluorescein and $700\ \text{nm}$ for NS), we were able to show prominent NS luminescence (emission peak at $610\ \text{nm}$) and fluorescein fluorescence (emission peak at $540\ \text{nm}$), respectively. Following image acquisition from the third group of mice, fluorescein and NS images (red channel for fluorescein and green channel for NS) were co-registered. Figure 7(a) shows the x-y image projected along the z-direction and Fig. 7(b) demonstrates the x-z image projected along the y-direction with field of view of $198\ \mu\text{m} \times 198\ \mu\text{m} \times 80\ \mu\text{m}$. x-y images were taken from the site where a blood vessel was shown ($0\ \mu\text{m}$ in Fig. 7(b)) and down to $80\ \mu\text{m}$. Figure 7(c)–(f) present 3D images at different rotational angles. We found that NS were located close to the blood vessels, which provides clear visualization of how the poorly defined vasculature system affects accumulation of NS at the tumor site. These images indicate the application of TPIP for studying NS targeting kinetics in three-dimensions.

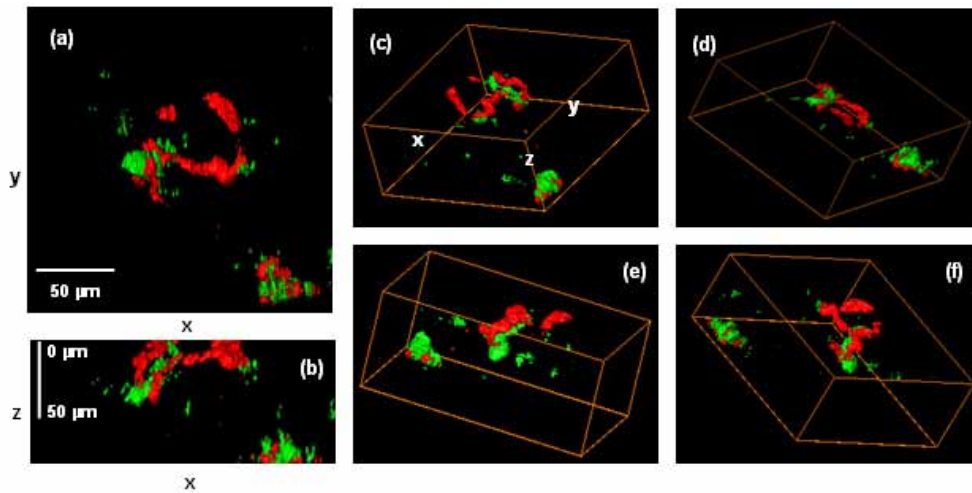


Fig. 7. 3D visualization of nanoshells (green) and blood vessels (red) in tumor. (a) z-projection of x-y images from tumor. (red: fluorescein in blood vessels, green: gold nanoshells) (b) y-projection of x-z images with field of view $198\ \mu\text{m} \times 80\ \mu\text{m}$. (c)–(f) 3D images of nanoshells in tumor at different rotational angles (c: movie file, 1.85 MB). (Scale bar: $50\ \mu\text{m}$ (a, b))

4. Conclusions

In conclusion, we have shown that NS yield a strong TPIP signal and have demonstrated the first direct luminescence-based contrast imaging of NS in bulk tissue. TPIP was verified by a quadratic dependence of TPIP emission intensity on the excitation power and the luminescence emission spectrum was found to be consistent with that from roughened gold surfaces. To demonstrate its use for imaging, we obtained TPIP images from subcutaneous tumors using a multi-photon microscope with a 780 nm excitation wavelength. By utilizing 3D data visualization software, 3D luminescence images were successfully demonstrated, which can be an attractive method to investigate the distribution and tumor targeting kinetics of NS. Our study suggests that TPIP imaging can hold an invaluable and promising position in understanding the transport kinetics of bioconjugated NS with cancer targeting biomarkers as well as imaging applications and will continue expanding its repertoire as a novel and effective imaging technique.